LEAST-SQUARES REVERSE-TIME MIGRATION TOWARD "TRUE" REFLECTIVITY

HAO ZHANG[1], QIANCHENG LIU[1*] and JUN HAO[2]

[1] *Key Laboratory of Petroleum Resources Research, Institute of Geology and Geophysics, Chinese Academy of Sciences, Beijing 100029,China, P.R. China. zhanghao@mail.iggcas.ac.cn*
[*] *Present address: King Abdullah University of Science and Technology, Thuwal, Saudi Arabia. liuqc@mail.iggcas.ac.cn*
[2] *Research Institute of Petroleum Exploration & Development, PetroChina, Qinghai, P.R. China. 407304895@qq.com*

(Received February 16, 2016; revised version accepted January 10, 2017)

ABSTRACT

Zhang, H., Liu, Q. and Hao, J., 2017. Least-squares reverse-time migration toward "true" reflectivity. *Journal of Seismic Exploration*, 26: 183-198.

Conventional least-squares reverse time migration (LSRTM) usually aims to improve the quality of seismic image, by removing the acquisition footprint, suppressing migration artifacts, and enhancing resolution. We find that the conventional reflectivity defined in the LSRTM is related to the normal-incidence reflection coefficient and the background velocity . Compared with the defined reflectivity, our inverted result is approximate. With reflected data, LSRTM is mainly sensitive to impedance perturbations. According to an approximate relationship between them, we reformulate the perturbation-related system into a pseudo reflection-coefficient related one. Then, we seek the inverted image through linearized iteration. With the assumption that the density varies gradually compared to the migration velocity, only the knowledge of the velocity is required, although the reflected waves are produced at impedance discontinuities. We validate our scheme using the 2D Marmousi synthetic dataset.

KEY WORDS: LSRTM, linear inversion, normal-incidence reflection coefficient.

INTRODUCTION

Reverse-time migration (RTM) is recognized as a state-of-the-art technology to image increasingly complicated subsurface structures. However, RTM is often implemented as an adjoint operator (Claerbout, 1992), which produces images of insufficient quality. Least-squares migration (LSM) can

0963-0651/17/$5.00

significantly improve the image quality, including suppressing migration artifacts, removing the acquisition footprint, balancing the source illumination, and enhancing resolution.

By linearized iterations, LSM attempts to seek the appropriate inverse operator. The LSM method was first applied to Kirchhoff migration (Nemeth et al., 1999; Duquet et al., 2000), then adapted to phase-shift migration (Kuehl and Sacchi, 2002; Clapp et al., 2005; Kaplan et al., 2010; Huang and Schuster, 2012) and one-way wave equation migration (Wang et al., 2005; Wang and Sacchi, 2007; Tang, 2008), and is now implemented with RTM (Dai and Schuster, 2010; Wong et al., 2010; Dai and Schuster, 2013; Tan and Huang, 2014; Dutta and Schuster, 2014; Zhang et al., 2015).

Governed by the two-way wave-equation, least-squares reverse-time migration (LSRTM) is able to handle complicated reflected waves. Under the acoustic assumption, according to the Born approximation, the true velocity and density models can be separated into the corresponding low-wavenumber backgrounds and high-wavenumber perturbations. The background velocity provides the kinematic information required to focus the waves to the scattering points. LSRTM aims to seek the high-wavenumber reflectivity, which may differ in physical definitions. Plessix and Li (2013) present a scheme to estimate the "relative impedance perturbation", assuming the velocity and impedance models are known. Zhang et al. (2014) estimate impedance and velocity perturbations, with the knowledge of background velocity and density. Because our scheme aims to improve the quality of stacked image rather than angle domain common image gather (Kuehl and Sacchi, 2002), the reflectivity defined here is related to the normal-incidence reflection coefficient model (Claerbout, 1992), which can be regarded as a relative reflectivity. In this paper, we find that although the reflected waves are generated at the impedance discontinuities, our inversion result is independent of the background density model. That is, only a kinematically correct background migration velocity is required as the starting model in our reflectivity inversion. In this paper, "kinematically correct" means that the background velocity should correctly predict the traveltimes of reflected waves (Virieux and Operto, 2009) within a half wavelength (Mora, 1987; Mora, 1989; Dai and Schuster, 2013) to prevent cycle-skipping.

The paper is arranged as follows. Firstly, we formulate the forward operator, and the reverse-time demigration (RTDM) system, where the defined reflectivity is related to the normal-incidence reflection coefficient model. Then, the adjoint operator, the reverse-time migration (RTM) system, is introduced. Then, the linearized inversion is reviewed, followed by the numerical implementation. Finally, we demonstrate our proposed scheme using the 2D Marmousi synthetic dataset.

METHODOLOGY

A forward operator, its adjoint operator, and the linearized inversion are required in LSRTM. In this section, we first formulate our forward operator, RTDM, in which the effective reflectivity is related to the normal-incidence reflection coefficient scaled by the background velocity and thus can be regarded as a relative reflectivity; then, we give the expression of the corresponding adjoint operator, RTM; finally, we briefly review the linearized inversion.

Reverse-time demigration formulations

In the time domain, the acoustic wave equation is

$$\{[1/v(\mathbf{x})^2](\partial^2/\partial t^2) - \rho(\mathbf{x})\nabla[1/\rho(\mathbf{x})]\cdot\nabla\}p(\mathbf{x},t) = s(t;\mathbf{x}_s) \quad , \tag{1}$$

where $v(\mathbf{x})$ denotes the velocity, $\rho(\mathbf{x})$ denotes the density, and $p(\mathbf{x},t;\mathbf{x}_s)$ denotes the pressure created by the source $s(t;\mathbf{x}_s)$ at $\mathbf{x}_s$. A true model can be separated into a background $v_0(x)$ and a perturbation $\delta v(x)$. If we define $\delta v(\mathbf{x}) = v(\mathbf{x}) - v_0(\mathbf{x})$, and $\delta\rho(\mathbf{x}) = \rho(\mathbf{x}) - \rho_0(\mathbf{x})$, the velocity and density terms in eq. (1) can be expanded as

$$1/[v_0(\mathbf{x}) + \delta v(\mathbf{x})]^2 = [1/v_0(\mathbf{x})^2] - [2\delta v(\mathbf{x})/v_0(\mathbf{x})^3] + O[\delta v(\mathbf{x})^2] \quad , \tag{2}$$

and

$$1/[\rho_0(\mathbf{x}) + \delta\rho(\mathbf{x})] = [1/\rho_0(\mathbf{x})] - [\delta\rho(\mathbf{x})/\rho_0(\mathbf{x})^2] + O[\delta\rho(\mathbf{x})^2] \quad . \tag{3}$$

Then, the zero-order and first-order approximation equations, obtained from eq. (1), can be, respectively, expressed as

$$\{[1/v_0(\mathbf{x})^2](\partial^2/\partial t^2) - \rho_0(\mathbf{x})\nabla[1/\rho_0(\mathbf{x})]\cdot\nabla\}p_0(\mathbf{x},t) = s(t;\mathbf{x}_s) \quad , \tag{4}$$

$$\{[1/v_0(\mathbf{x})^2](\partial^2/\partial t^2) - \rho_0(\mathbf{x})\nabla[1/\rho_0(\mathbf{x})]\cdot\nabla\}\delta p(\mathbf{x},t)$$

$$= \{[2\delta v(\mathbf{x})/v_0(\mathbf{x})^3](\partial^2/\partial t^2) - \nabla[\delta\rho(\mathbf{x})/\rho_0(\mathbf{x})]\cdot\nabla\}p_0(\mathbf{x},t) \quad , \tag{5}$$

where $p_0(\mathbf{x})$ is the incident wavefield, $\delta p(\mathbf{x}) = p(\mathbf{x}) - p_0(\mathbf{x})$ is the secondary reflected wavefield caused by model perturbations $\delta v(\mathbf{x})$ and $\delta\rho(\mathbf{x})$. The demigration operator consists of eqs. (4) and (5). The wavefield perturbation $\delta\rho(\mathbf{x})$ recorded at $\mathbf{x}_R$ is the demigrated data: $d(\mathbf{x}_R,t) = \delta p(\mathbf{x}_R,t)$. Because the background density $\rho_0(\mathbf{x})$ is continuous and varies more gradually than the background velocity $v_0(\mathbf{x})$, the term $\rho_0(\mathbf{x})\nabla[1/\rho_0(\mathbf{x})]\cdot\nabla$ approximately reduces to ∇^2. However, there are still two different perturbations $\delta v(\mathbf{x})$ and $\delta\rho(\mathbf{x})$ and two different backgrounds $v_0(\mathbf{x})$ and $\rho_0(\mathbf{x})$ existing in the right-hand side of eq. (5). It is more challenging to estimate the density model $\rho_0(\mathbf{x})$ than the migration velocity $v_0(\mathbf{x})$.

Our LSRTM is proposed here to improve the quality of the stacked image rather than to obtain angle-domain common imaging gathers. As shown in Appendix A, assuming the background density is continuous, we prove that eqs. (4) and (5) can be rewritten as

$$\begin{cases} \{[1/v_0(\mathbf{x})^2](\partial^2/\partial t^2) - \nabla^2\}p_0(\mathbf{x},t) = s(t;\mathbf{x}_s) \ , \\ \{[1/v_0(\mathbf{x})^2](\partial^2/\partial t^2) - \nabla^2\}\delta p(\mathbf{x},t) = m(\mathbf{x})[\partial p_0(\mathbf{x},t)/\partial t] \ . \end{cases} \tag{6}$$

The reflectivity model defined here is $m(\mathbf{x}) = 4r(\mathbf{x})/v_0(\mathbf{x})$, where $r(\mathbf{x})$ denotes the normal-incidence reflection coefficient model. Like the amplitude, it is a relative conception rather than the true reflectivity model. We call this the relative reflectivity or scaled reflectivity. The demigration system (6) looks similar to the demigration system in Zhang et al., (2015), except for an additional scaling of $4/v_0(\mathbf{x})$. System (6) indicates that although the reflected waves are generated at impedance discontinuities, it is reasonable to seek $m(\mathbf{x})$ even without the knowledge of $\rho_0(\mathbf{x})$. Moreover, because the observed data are generated from eq. (1) and the density term is neglected in system (6), the inverted result is relatively correct in the linearized inversion using LSRTM rather than FWI. That is the reason that we use the so-called "true" reflectivity. For simplicity, the solution of the demigration system (6) can be represented in a compact matrix form $\mathbf{d} = \mathbf{Lm}$, where $\mathbf{d}$ denotes the demigrated data δp recorded at receivers $\mathbf{x}_R$, $\mathbf{L}$ denotes the demigration operator, $\mathbf{m}$ denotes the reflectivity model.

Reverse-time migration formulations

According to the adjoint-state method (Claerbout, 1992; Plessix, 2006), as shown in Appendix B, the reverse-time migration system, i.e., the adjoint of system (6), can be expressed as

$$\begin{cases} \{[1/v_0(\mathbf{x})^2](\partial^2/\partial t^2) - \nabla^2\}p_S(\mathbf{x},t) = s(t;\mathbf{x}_s) \ , \\ \{[1/v_0(\mathbf{x})^2](\partial^2/\partial t^2) - \nabla^2\}p_R(\mathbf{x},t) = -\partial\tilde{d}(\mathbf{x}_R,t)/\partial t \ , \end{cases} \tag{7}$$

where $p_S(\mathbf{x},t)$ denotes the forward propagated source wavefield, and $p_R(\mathbf{x},t)$ denotes the backward propagated receiver wavefield. Applying the cross-correlation imaging condition yields

$$\tilde{m}(\mathbf{x}) = \int\int p_R(\mathbf{x},t;\mathbf{x}_S)p_S(\mathbf{x},t;\mathbf{x}_S)d\mathbf{x}d\mathbf{x}_S \ . \tag{8}$$

Then, the stacked image $\tilde{m}(\mathbf{x})$ is normalized by smoothing the sum of source illumination (Guitton et al., 2007), rather than by the source illumination

shot-by-shot, to compensate for the geometric spreading. In this case, the near-incidence imaging energy is enhanced (Beylkin et al., 1985), and it is reasonable to approximate the near-incidence reflection coefficient with the normal-incidence reflection coefficient. For simplicity, the solution of the migration system (7) can be represented in a compact matrix form $\mathbf{m} = \mathbf{L}^T\mathbf{d}$, where $\mathbf{d}$ denotes the observed data $\tilde{d}$ recorded at receivers $\mathbf{x}_R$, $\mathbf{L}^T$ denotes the migration operator, and $\mathbf{m}$ denotes migrated image.

Linearized inversion

LSRTM aims to solve the reflectivity model m($\mathbf{x}$) by minimizing the least-squares function:

$$F(\mathbf{m}) = \tfrac{1}{2} \sum_{i=1}^{N_S} \| \mathbf{L}_i\mathbf{m} - \mathbf{d}_i \|_2^2 + (\alpha/2) \sum_{i=1}^{N_S} \| \mathbf{m} \|_2^2 , \tag{9}$$

where $\mathbf{L}$ represents the forward modeling operator describing the demigration system in system (6), $\mathbf{m}$ is defined as the stacked migration image, N_S denotes the number of shots, $(\alpha/2) \sum_{i=1}^{N_S} \| \mathbf{m} \|_2^2$ is the regularization term and α is chosen empirically. To minimize $F(\mathbf{m})$ in eq. (9), we pursue the negative direction of the gradient

$$\partial F(\mathbf{m})/\partial \mathbf{m} = \sum_{i=1}^{N_S} \mathbf{L}_i^T(\mathbf{L}_i\mathbf{m} - \mathbf{d}_i) + \sum_{i=1}^{N_S} \alpha\mathbf{m} , \tag{10}$$

where $\mathbf{L}^T$ denotes the adjoint of the forward modeling operator (Claerbout, 1992) describing the migration system (7), $\mathbf{Lm} - \mathbf{d}$ denotes the residual between predicted data and observed data. Then, the inverted reflectivity can be approached by migrating the residuals iteratively. The numerical solution of LSRTM can be found using the conjugate gradient algorithm (Nemeth et al., 1999).

NUMERICAL IMPLEMENTATION

The proposed scheme that handles LSRTM toward the "true" reflectivity can be performed as follows:

1. Demigrate the formerly inverted image to produce the demigrated data.

2. Backward propagate the residual between the observed data and the demigrated data and cross-correlate with the source wavefield.

3. Stack the migration results over shots to produce a gradient.

4. Perform an update of the inverted image using the conjugate gradient method to minimize the objective function.

5. Check the objective function and the stopping criterion. Either stop here or repeat steps from one to four.

NUMERICAL EXAMPLES

Four-layer model

A simple model is used to illustrate our scheme. The true velocity model contains four layers with velocities of 1500 m/s, 2000 m/s, 1750 m/s, and 2250 m/s (Fig. 1a). The true densities of the same four layers are 850 kg/m^3, 800 kg/m^3, 1050 kg/m^3, and 1000 kg/m^3 (Fig. 1b). The corresponding impedance model is shown in Fig. 1c. Synthetic data are generated with single acquisition geometry for one source in the center of the acquisition aperture. 301 receivers are located on the surface of the model with a 5-m interval. A Ricker wavelet with a peak-frequency of 20 Hz is the source function.

In our LSRTM, only the migration velocity (Fig. 2a) is required. Compared with the conventional RTM image in Fig. 2b, the quality of the LSRTM image in Fig. 2c is significantly improved. Moreover, as shown in Fig. 3, the LSRTM image approaches the "true" reflectivity.

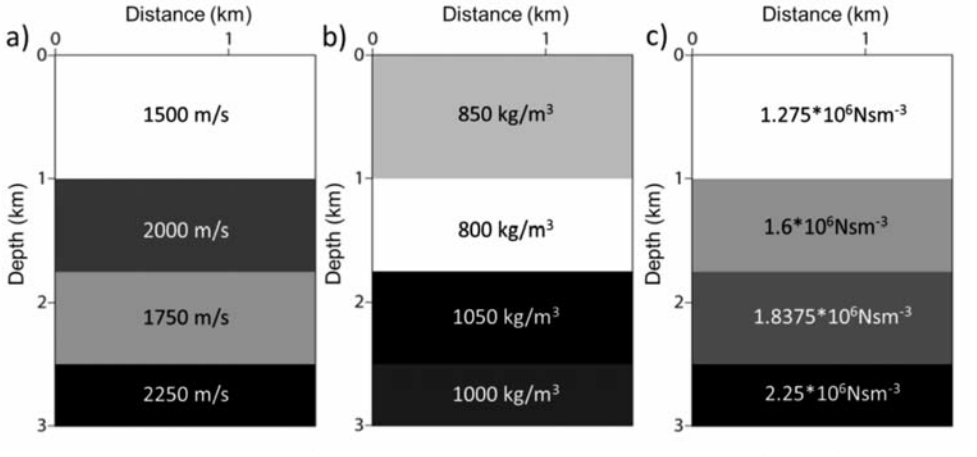

Fig. 1. (a) The four-layer velocity model. (b) The four-layer density model. (c) The corresponding impedance model. The observed data in our LSRTM is generated using (a) and (b).

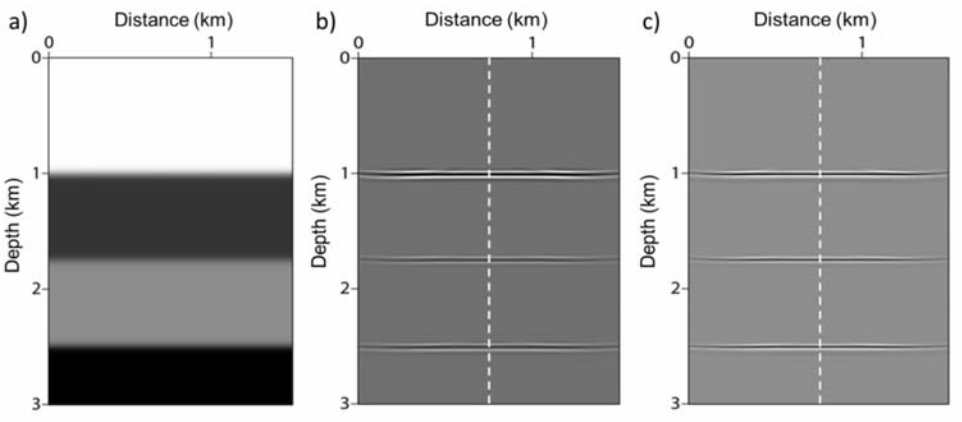

Fig. 2. (a) The background velocity used in our LSRTM. (b) The conventional RTM image. (c) The LSRTM image. In part (c), the imaging amplitudes are balanced, and the resolution is enhanced.

Marmousi model evaluation

We evaluate our scheme using the 2D Marmousi model. The true velocity and density models are illustrated in Figs. 4a and 4b. The synthetic dataset is generated using an $O(dt^2,dx^4)$ staggered-grid finite-difference stencil (Virieux, 1987). In the acquisition geometry, 150 shots are excited at an interval of 50 m, and 801 receivers are deployed with a 5-m interval for each shot. A synthetic dataset at shot location 3 km is shown in Fig. 5a. A Ricker wavelet with a 20 Hz peak frequency is used, and the recording duration is 4 s. The smoothed migration velocity (Fig. 4c), is achieved by a two-sided exponential smoothing filter with a window length of 100 m to blur the subtle details of true velocity. Fig. 6a depicts the true reflectivity related to the normal-incidence reflection-coefficient model and the background velocity.

After 20 iterations, we obtain the inverted LSRTM image in Fig. 6c. Compared to the conventional RTM image in Fig. 6b, the amplitudes of the reflectors are balanced, and the image resolution is enhanced. The demigrated data at the shot location at 3 km, from the final inverted image, is shown in Fig. 5b. The data residual is depicted in Fig. 5c. We observed that the demigrated data approaches the synthetic data well. However, since LSRTM aims to invert the high-wavenumber reflectivity, there are some low-frequency data residuals in Fig. 5c.

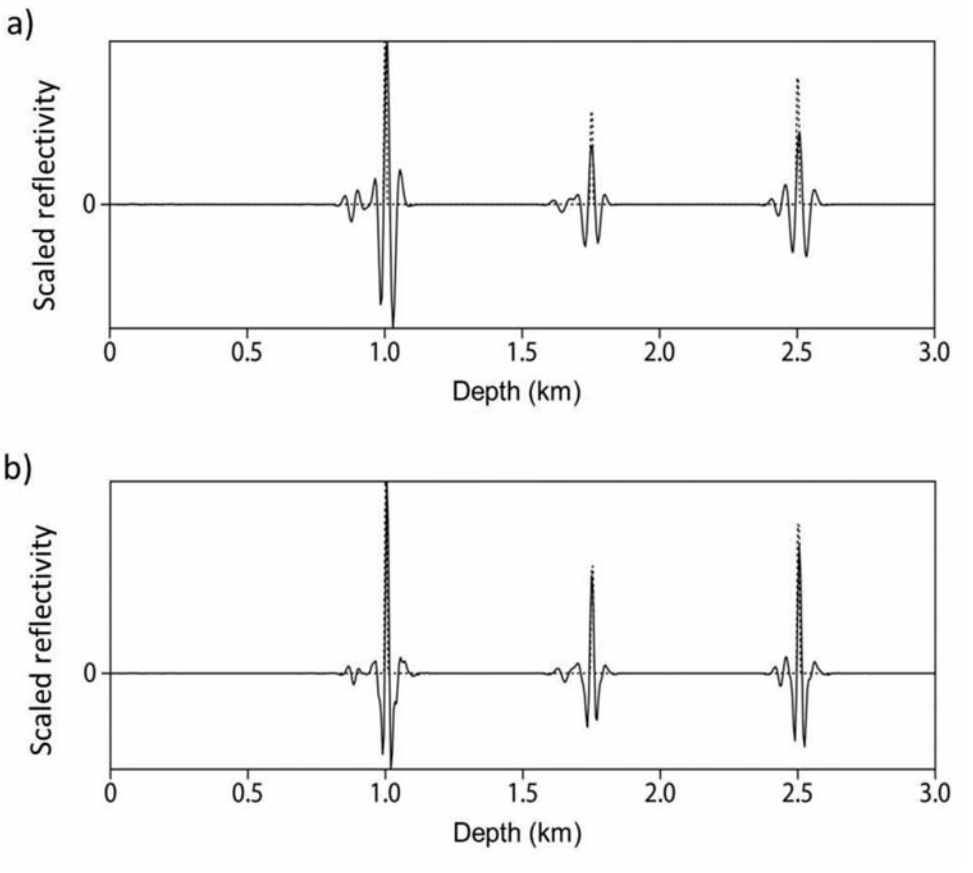

Fig. 3. The comparison between the computed reflectivity curves (a) and (b) from Figs. 2b and 2c at distance 0.75 km, respectively. The dashed lines are the reflectivity curves defined as $m(\mathbf{x}) = r(\mathbf{x})/v_0(\mathbf{x})$ for reference. Here, $r(\mathbf{x})$ is the normal-incidence reflection coefficient estimated from Fig. 1c, and $v_0(\mathbf{x})$ is the background velocity in Fig. 2a. Although the reflected waves are generated at the impedance discontinuities of Fig. 1c, only $v_0(\mathbf{x})$ is used to produce the relative scaled reflectivity.

In Fig. 6, we compare the initial stacked RTM image in Fig. 6b with the inverted LSRTM image after 20 iterations in Fig. 6c. Obviously, because least-squares solution implicitly aims to seek the inverse operator rather than the adjoint operator, LSRTM can gradually suppress the side lobes of RTM to achieve a high-resolution amplitude-balanced inversion result in Fig. 6c. Weak energies around the target reservoir at the depth of 2500 m are remarkably recovered and focused. More fine subsurface details are revealed.

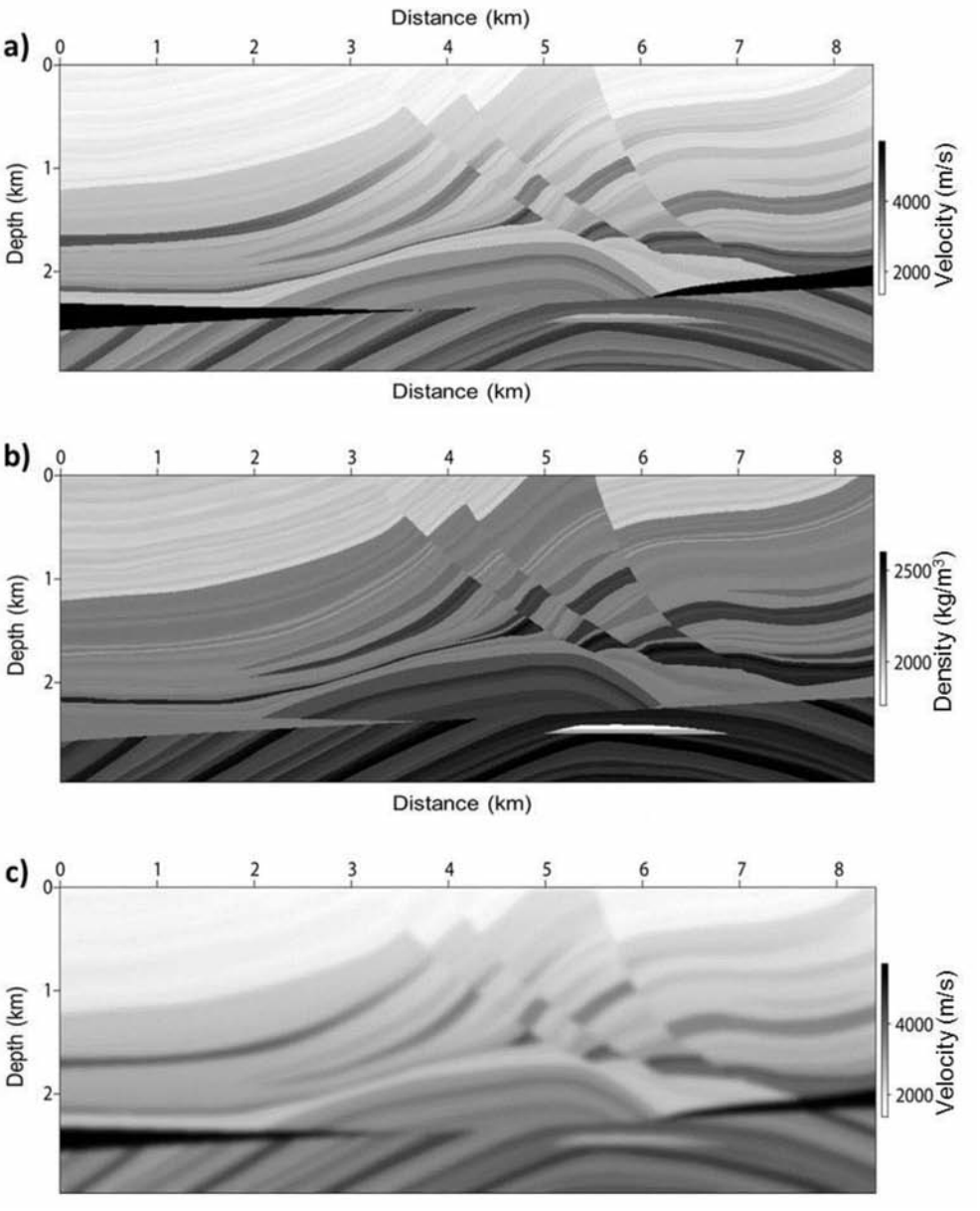

Fig. 4. (a) The true Marmousi velocity model. (b) The true Marmousi density model. (c) Smooth background velocity used in our LSRTM.

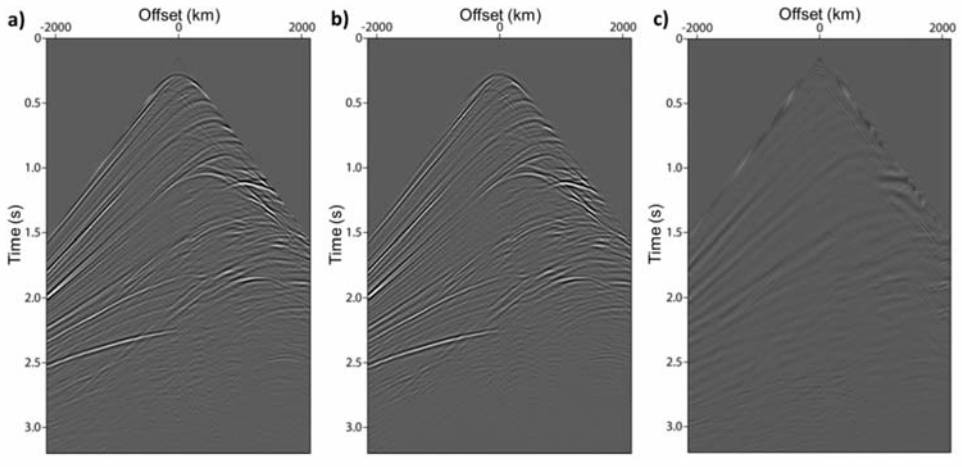

Fig. 5. (a) The observed data in our LSRTM is generated using the models in Figs. 4a and 4b, for a source at 3 km in Fig.4. (b) The demigrated data from the inverted reflectivity after 20 iterations. (c) Residual data between parts (a) and (b).

In Fig. 7, we compare the detailed traces extracted from Fig. 6c at distance 4 km, with the true reflectivity curve from Fig. 6a. The two curves look similar. This implies that our LSRTM is also a useful tool to compute the "true" reflectivity, which may help interpreters to characterize the reservoirs. Moreover, we demonstrate that although the reflected waves are produced at impedance discontinuities, it is reasonable to estimate the normal-incidence reflection coefficient related reflectivity model $m(\mathbf{x}) = 4r(\mathbf{x})/v_0(\mathbf{x})$ even without the knowledge of the background density model.

CONCLUSIONS

LSRTM is an effective technique for improving the imaging quality of RTM. In this paper, we find that the inverted high-wavenumber image approaches the "true" reflectivity. The stacked inverted image is closely related to the normal-incidence reflection coefficient model. Moreover, assuming the background density being continuous and varying more gradually, and that does not contribute to much to the reflectivity inversion, we demonstrate that although the reflected waves are generated at impedance discontinuities, only an accurate migration velocity model is required in our reflectivity inversion. Two numerical experiments have verified our scheme.

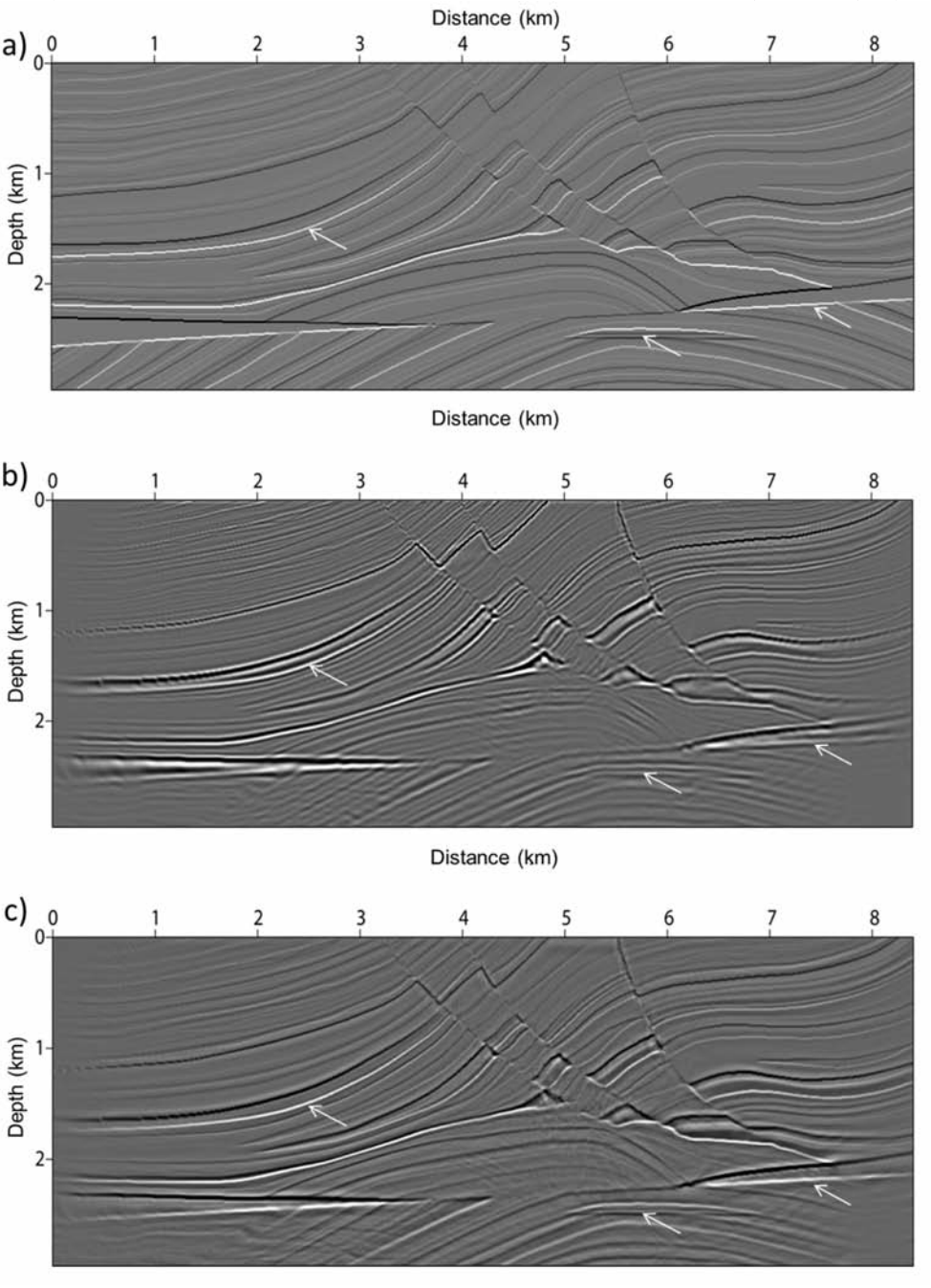

Fig. 6. (a) The true Marmousi reflectivity model defined as $m(\mathbf{x}) = r(\mathbf{x})/v_0(\mathbf{x})$ for reference. (b) The conventional stacked RTM image. (c) Our LSRTM inverted image. By comparing at the arrows, the image quality in part (c) is significantly improved.

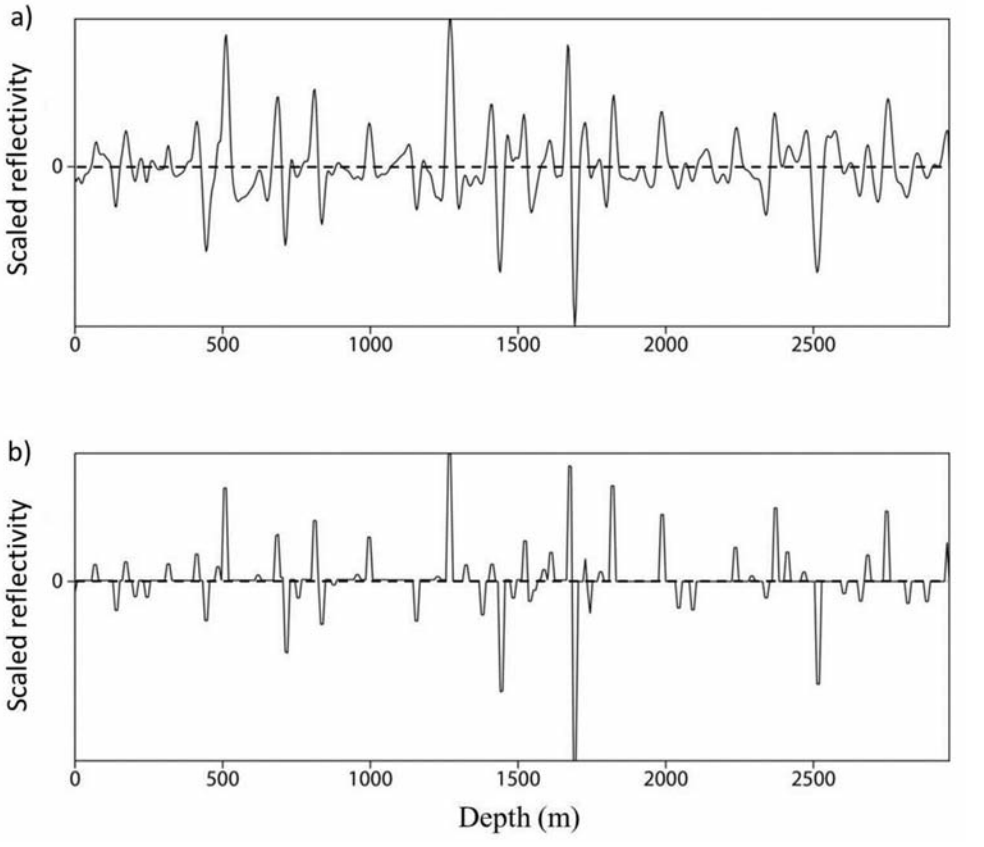

Fig. 7. (a) The detailed inverted reflectivity by our LSRTM. (b) The true detailed reflectivity $m(\mathbf{x}) = r(\mathbf{x})/v_0(\mathbf{x})$. Both they are extracted at the same location of distance 4 km from Figs. 6a and 6c.

ACKNOWLEDGEMENT

The authors are grateful to the National Natural Science Fund of China (under Grant No. 41574135) and to the National Major Project of China (under Grant No. 2016ZX05008-007) for supporting this work. We thank the reviewer Peter Mora for his constructive comments and textual suggestions that greatly improved the manuscript.

REFERENCES

Beylkin, G., Oristaglio, M. and Miller, D., 1985. Spatial resolution of migration algorithms. Acoust. Imag., 14: 155-168.

Claerbout, J.F., 1992. Earth Soundings Analysis. Processing Versus Inversion. Blackwell Science Pubications, Oxford.

Clapp, M.L., Clapp, R.G. and Biondi, B.L., 2005. Regularized least-squares inversion for 3-D subsalt imaging. Expanded Abstr., 75th Ann. Internat. SEG Mtg., Houston: 1814-1817.

Dai, W. and Schuster, G.T., 2013. Plane-wave least-squares reverse-time migration. Geophysics, 78(4): S165-S177.

Dutta, G. and Schuster, G.T., 2014. Attenuation compensation for least-squares reverse time migration using the visco-acoustic wave-equation. Geophysics, 79(6): S251-S262.

Guitton, A., Valenciano, A., Bevc, D. and Claerbout, J., 2007. Smoothing image condition for shot-profile migration. Geophysics, 72(3): S149-S154.

Huang, Y. and Schuster, G.T., 2012. Multisource least-squares migration of marine streamer data and land data with frequency-division encoding. Geophys. Prosp., 60: 663-680.

Kaplan, S.T., Routh, P.S. and Sacchi, M.D., 2010. Derivation of forward and adjoint operators for least-squares shot-profile split-step migration. Geophysics, 75(6): S225-S235.

Kuehl, H. and Sacchi, M.D., 2002. Robust AVP estimation using least-squares wave-equation migration. Expanded Abstr., 72nd Ann. Internat. SEG Mtg., Salt Lake City: 281-284.

Mora, P., 1987. Nonlinear two-dimensional elastic inversion of multi-offset seismic data. Geophysics, 52: 1211-1228.

Mora, P., 1989. Inversion = migration + tomography. Geophysics, 54: 1575-1586.

Lailly, P., 1984. The seismic inverse problem as a sequence of before stack migrations. Conf. Inverse Scatter., Theory and Application. Soc. Industr. Appl. Mathemat., 15: 206-220.

Nemeth, T., Wu, C. and Schuster, G.T., 1999. Least-squares migration of incomplete reflection data. Geophysics, 64: 208-221.

Plessix, R.E., 2006. A review of the adjoint-state method for computing the gradient of a functional with geophysical applications. Geophys. J. Internat., 167: 495-503.

Plessix, R.E. and Li, Y., 2013. Waveform acoustic impedance inversion with spectral shaping. Geophys. J. Internat., 195: 301-314.

Schuster, G.T., 1993. Least-squares crosswell migration. Expanded Abstr., 63rd Ann. Internat. SEG Mtg., Washington D.C.: 110-113.

Tan, S. and Huang, L., 2014. Least-squares reverse-time migration with a wavefield-separation imaging condition and updated source wavefields. Geophysics, 79(5): S195-S205.

Tang, Y., 2008. Wave-equation Hessian by phase encoding. Expanded Abstr., 78th Ann. Internat. SEG Mtg., Las Vegas: 2201-2205.

Ten Kroode, F., 2012. A wave-equation-based Kirchhoff operator. Inverse Probl., 28: 1-28.

Virieux, J., 1986. P-SV wave propagation in heterogeneous media, velocity-stress finite difference method. Geophysics, 51: 889-901.

Virieux, J. and Operto, S., 2009. An overview of full-waveform inversion in exploration geophysics. Geophysics, 74(6): WCC127-WCC152.

Wang, J., Kuehl, H. and Sacchi, M.D., 2005. High-resolution wave-equation AVA imaging: Algorithm and tests with a data set from the Western Canadian Sedimentary Basin. Geophysics, 70(5): S91-S99.

Wang, J. and Sacchi, M.D., 2007. High-resolution wave equation AVP imaging with sparseness constraints. Geophysics, 72(1): S11-S18.

Zhang, Y., Ratcliffe, A., Roberts, G. and Duan, L., 2014. Amplitude-preserving reverse time migration: From reflectivity to velocity and impedance inversion. Geophysics, 79(6): S271-S283.

Zhang, Y., Duan, L. and Xie, Y., 2015. A stable and practical implementation of least-squares reverse time migration. Geophysics, 80(1): V23-V31.

APPENDIX A

REVERSE-TIME DEMIGRATION SYSTEM

According to the Fredholm integral equation, from eqs. (4-5), the wavefield perturbation of shot $\mathbf{x}_S$ recorded at receiver position $\mathbf{x}_R$ can be expressed as

$$d(\mathbf{x}_R,\omega;\mathbf{x}_S) = \int \{[\delta\rho(\mathbf{x})/\rho_0(\mathbf{x})]\nabla\cdot[\delta G(\mathbf{x}_R,\omega;\mathbf{x}_S)\nabla G_0(\mathbf{x},\omega;\mathbf{x}_S)] - [2\omega^2\rho v(\mathbf{x})/v_0(\mathbf{x})^3]G_0(\mathbf{x},\omega;\mathbf{x}_S)\delta G(\mathbf{x}_R,\omega;\mathbf{x}_S)\}d\mathbf{x} \quad . \tag{A-1}$$

Asymptotically, the background and perturbation waves, respectively, can be expressed as

$$G_0(\mathbf{x},\omega;\mathbf{x}_S) = A(\mathbf{x};\mathbf{x}_S)e^{i\omega\tau(\mathbf{x};\mathbf{x}_S)} \quad , \tag{A-2}$$

and

$$\delta G(\mathbf{x}_R,\omega;\mathbf{x}) = A(\mathbf{x}_R;\mathbf{x}_S)e^{i\omega\tau(\mathbf{x}_R;\mathbf{x})} \quad . \tag{A-3}$$

The gradients of eqs. (A-2) and (A-3) are

$$\nabla G_0(\mathbf{x},\omega;\mathbf{x}_S) \approx i\omega\nabla\tau(\mathbf{x};\mathbf{x}_S)A(\mathbf{x};\mathbf{x}_S)e^{i\omega\tau(\mathbf{x};\mathbf{x}_S)} \quad , \tag{A-4}$$

and

$$\nabla\delta G(\mathbf{x}_R,\omega;\mathbf{x}) \approx i\omega\nabla\tau(\mathbf{x}_R;\mathbf{x})A(\mathbf{x}_R;\mathbf{x})e^{i\omega\tau(\mathbf{x}_R;\mathbf{x})} \quad . \tag{A-5}$$

Substituting eqs. (A-4) and (A-5) into eq. (A-1), at near-offset,

$$d(\mathbf{x}_R,\omega;\mathbf{x}_S) = -\int [2\omega^2/v_0(\mathbf{x})^2]\{[\delta v(\mathbf{x})/v_0(\mathbf{x})] + [\delta\rho(\mathbf{x})/\rho_0(\mathbf{x})]\} \times A(\mathbf{x}_R;\mathbf{x})A(\mathbf{x};\mathbf{x}_S)e^{i\omega[\tau(\mathbf{x};\mathbf{x}_S)+\tau(\mathbf{x}_R;\mathbf{x})]}d\mathbf{x} \quad , \tag{A-6}$$

which denotes the relationship between the data perturbation and the model perturbation. A concrete form of the model perturbation $\delta\tilde{m}(\mathbf{x})$ is

$$\delta\tilde{m}(\mathbf{x}) = [\delta v(\mathbf{x})/v_0(\mathbf{x})] + [\delta\rho(\mathbf{x})/\rho_0(\mathbf{x})] = \delta[\rho(\mathbf{x})v(\mathbf{x})]/[\rho_0(\mathbf{x})v_0(\mathbf{x})] = \delta[Z(\mathbf{x})]/Z_0(\mathbf{x}) \quad , \tag{A-7}$$

where $Z(\mathbf{x}) = \delta(\mathbf{x})v(\mathbf{x})$ denotes the impedance model. Ten Kroode (2012) introduces an approximate relationship between the model perturbation $\delta\tilde{m}(\mathbf{x})$ and the reflection coefficient $r(\mathbf{x})$, for the near-offsets case, which can be expressed as

$$r(\mathbf{x}) = [i\omega/2v_0(\mathbf{x})][\delta Z(\mathbf{x})/Z_0(\mathbf{x})] = [i\omega/2v_0(\mathbf{x})]\delta\tilde{m}(\mathbf{x}) \quad . \tag{A-8}$$

Substituting eq. (A-8) into eq. (A-6), we have

$$d(\mathbf{x}_R,\omega;\mathbf{x}_S) \approx \int i\omega[4(\mathbf{x})/v_0(\mathbf{x})]A(\mathbf{x}_R;\mathbf{x})A(\mathbf{x};\mathbf{x}_S)e^{i\omega[\tau(\mathbf{x};\mathbf{x}_S)+\tau(\mathbf{x}_R;\mathbf{x})]}\,d\mathbf{x}. \tag{A-9}$$

Finally, from eq. (A-9), the reverse-time demigration system, eqs (4-5), can be written as

$$\begin{cases} \{[1/v_0(\mathbf{x})^2](\partial^2/\partial t^2) - \nabla^2\}p_0(\mathbf{x},t) = s(t;\mathbf{x}_s) \quad , \\ \{[1/v_0(\mathbf{x})^2](\partial^2/\partial t^2) - \nabla^2\}\delta p(\mathbf{x},t) = [4r(\mathbf{x})/v_0(\mathbf{x})][\partial p_0(\mathbf{x},t)/\partial t] \quad , \\ d(\mathbf{x}_R,t) = \delta p(\mathbf{x}_R,t) \quad . \end{cases} \tag{A-10}$$

Here, the reflectivity related to the normal-incidence reflection coefficient is defined as

$$m(\mathbf{x}) = 4r(\mathbf{x})/v_0(\mathbf{x}) \quad . \tag{A-11}$$

APPENDIX B

REVERSE-TIME MIGRATION SYSTEM

Eq. (A-10) is the forward operator defined as $d(\mathbf{x}_R,t;\mathbf{x}_S) = L[m(\mathbf{x})]$. Now we try to find the transpose operator $\tilde{m}(\mathbf{x}) = L^T[\tilde{d}(\mathbf{x}_R,t;\mathbf{x}_S)]$. According to the dot product test (Claerbout, 1992), for a function $d(\mathbf{x}_R,t;\mathbf{x}_S)$ in the data domain, the transpose operator $\tilde{m}(\mathbf{x})$ is defined as

$$\int \tilde{m}(\mathbf{x})\cdot m(\mathbf{x})d\mathbf{x} = \int\int\int \tilde{d}(\mathbf{x}_R,\omega;\mathbf{x}_S)\cdot d(\mathbf{x}_R,\omega;\mathbf{x}_S)d\mathbf{x}_R d\omega d\mathbf{x}_S \quad . \tag{B-1}$$

Eq. (A-10) can be written as

$$d(\mathbf{x}_R,\omega;\mathbf{x}_S) = \int\int i\omega m(\mathbf{x})G_R(\mathbf{x}_R,\omega;\mathbf{x})G_S(\mathbf{x},\omega;\mathbf{x}_S)d\omega d\mathbf{x}_S \quad , \tag{B-2}$$

where $G_R(\mathbf{x}_R,\omega;\mathbf{x})$ and $G_S(\mathbf{x},\omega;\mathbf{x}_S)$ denote the receiver and source wavefields, respectively. Substituting eq. (B-2) into eq. (B-1),

$$\tilde{m}(\mathbf{x}) = \int\int\int -i\omega\tilde{d}(\mathbf{x}_R,\omega;\mathbf{x}_S)G_R(\mathbf{x},\omega;\mathbf{x}_R)G_S(\mathbf{x},\omega;\mathbf{x}_S)d\omega d\mathbf{x}_R d\mathbf{x}_S \quad . \tag{B-3}$$

Finally, the transpose operator, the reverse-time migration system, can be written as

$$\begin{cases} \{[1/v_0(\mathbf{x})^2](\partial^2/\partial t^2) - \nabla^2\}p_S(\mathbf{x},t) = s(t;\mathbf{x}_s) \quad , \\ \{[1/v_0(\mathbf{x})^2](\partial^2/\partial t^2) - \nabla^2\}p_R(\mathbf{x},t) = -[\partial\tilde{d}(x_R,t;x_s)/\partial t] \quad . \end{cases} \tag{B-4}$$

Applying the cross-correlation imaging condition for all shots yields

$$\tilde{m}(\mathbf{x}) = \int\int p_R(\mathbf{x},t;\mathbf{x}_S)p_S(\mathbf{x},t;\mathbf{x}_S)dtd\mathbf{x}_S \quad . \tag{B-5}$$